

## Supporting Information

### **Decoration of Co/Co<sub>3</sub>O<sub>4</sub> nanoparticles with Ru nanoclusters: A new strategy for design of highly-active hydrogenation**

Lihua Zhu,<sup>a</sup> Zhiqing Yang,<sup>b,\*</sup> Jinbao Zheng,<sup>a,\*</sup> Weiwei Hu,<sup>b</sup> Nuwei Zhang,<sup>a</sup> Yunhua Li,<sup>a</sup> Chuan-Jian Zhong,<sup>c</sup> Hengqiang Ye<sup>b</sup> and Bing H Chen<sup>a,\*</sup>

<sup>a</sup> Department of Chemical and Biochemical Engineering, National Engineering Laboratory for Green Productions of Alcohols-Ethers-Esters, College of Chemistry and Chemical Engineering, Xiamen University, Xiamen 361005, China

<sup>b</sup> Shenyang National Laboratory for Materials Science, Institute of Metal Research, Chinese Academy of Sciences, Shenyang 110016, China

<sup>c</sup> Department of Chemistry, State University of New York at Binghamton, Binghamton, New York 13902, United States

#### **Corresponding Author**

[yangzq@imr.ac.cn](mailto:yangzq@imr.ac.cn) ; [jbzheng@xmu.edu.cn](mailto:jbzheng@xmu.edu.cn) ; [chenbh@xmu.edu.cn](mailto:chenbh@xmu.edu.cn)

## Supporting Information

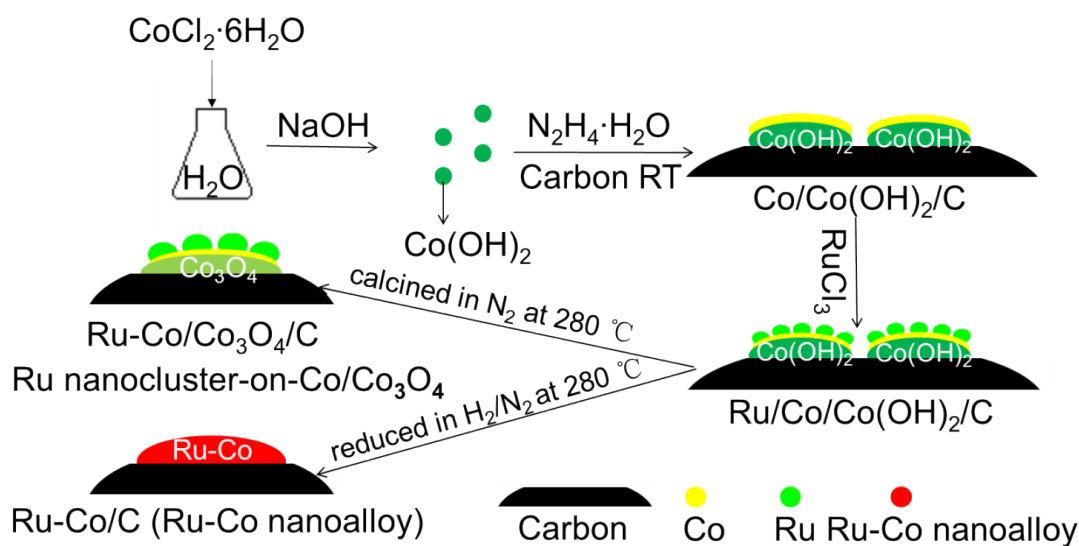
### 1. Experimental Details

#### (1) Preparation of catalysts

The carbon-supported Co/Co(OH)<sub>2</sub> was prepared at RT via hydrazine hydrate reduction method. The main steps were described below, 12.5 mL of anhydrous ethanol were added into 82.5 mL of an aqueous cobalt(II) chloride hexahydrate (CoCl<sub>2</sub>·6H<sub>2</sub>O) solution, and stirred at RT for ten minutes. Then 12.5 mL of aqueous NaOH (1.813 g) solution was placed into the above liquid. Ten minutes later, 25 mL of 85 wt% hydrazine hydrate solution was added into the as-obtained liquid. Subsequently, 1.250 g of carbon black (approximately S<sub>BET</sub> = 1385.3 m<sup>2</sup> g<sup>-1</sup>) was mixed with the solution, and transferred into a Teflon cup. After 18 hours of vigorous agitation at RT. The solid product (Co/Co(OH)<sub>2</sub>/C) was acquired by filtration, thoroughly washed with deionized water and anhydrous ethanol and dried overnight in vacuum. Co/Co<sub>3</sub>O<sub>4</sub>/C was obtained after Co/Co(OH)<sub>2</sub>/C annealed in flowing N<sub>2</sub> of 80 mL min<sup>-1</sup> at 280 °C for 3 h. And Co loading (total Co element) of Co/Co<sub>3</sub>O<sub>4</sub>/C was 2.8 wt% obtained by ICP-MS. Ru/Co/Co(OH)<sub>2</sub>/C was synthesized via galvanic replacement reaction (adding Co/Co(OH)<sub>2</sub>/C into an aqueous solution of RuCl<sub>3</sub> (9.64×10<sup>-3</sup> mol L<sup>-1</sup>) and subsequently dried in a vacuum oven at 60 °C for 6 h. The Ru/Co/Co<sub>3</sub>O<sub>4</sub>/C and Ru-Co/C catalysts were obtained after Ru/Co/Co(OH)<sub>2</sub>/C annealed in flowing N<sub>2</sub> or N<sub>2</sub>+10%H<sub>2</sub> of 80 mL min<sup>-1</sup> at 280 °C for 3 h, respectively (Scheme S1). Ru/C was synthesized via incipient wetness impregnation and then reduced in flowing N<sub>2</sub>+10%H<sub>2</sub> of 80 mL min<sup>-1</sup> at 380 °C for 3 h. The rate of heating was 2°C min<sup>-1</sup>. The Ru/C catalyst with Ru loading of 1.25 wt% was determined by ICP-MS.

The process for the synthesis of the Ru/Co/Co<sub>3</sub>O<sub>4</sub>/C and Ru-Co/C catalysts is shown in Scheme S1. Firstly, Co<sup>2+</sup> ions reacted with OH<sup>-</sup> ions, forming Co(OH)<sub>2</sub>; secondly, a small amount of Co<sup>2+</sup> ions via the dissociation of Co(OH)<sub>2</sub> were reduced to Co(0) at RT by hydrazine hydrate, supported on Co(OH)<sub>2</sub>. The limited concentration of free Co<sup>2+</sup> ions led to a relatively slow growing rate of Co NPs, and

then  $\text{Co}/\text{Co}(\text{OH})_2$  was loaded on carbon; finally,  $\text{Ru}/\text{Co}/\text{Co}(\text{OH})_2/\text{C}$  was obtained after some of Co atoms displaced with Ru atoms via galvanic replacement reaction. And, the  $\text{Ru}/\text{Co}/\text{Co}_3\text{O}_4/\text{C}$  and  $\text{Ru-Co}/\text{C}$  catalysts will be obtained under various thermal treatment conditions. The  $\text{Ru}/\text{Co}/\text{Co}_3\text{O}_4/\text{C}$  and  $\text{Ru-Co}/\text{C}$  catalysts were with 1.25 wt% Ru loading and 1.40 wt% total Co loading analyzed by ICP-MS.



**Scheme S1.** Schematic illustration for the preparation process of the  $\text{Ru}/\text{Co}/\text{Co}_3\text{O}_4/\text{C}$  and  $\text{Ru-Co}/\text{C}$  catalysts.

## (2) Characterization

Thermal-gravity (TG) test was performed on TG 209F1 thermal gravimeter. About 0.3000 mg of sample was used in each test. The flowing rate of 99.999% $\text{N}_2$  was  $20 \text{ mL min}^{-1}$ , with heating rate of  $10^\circ\text{C min}^{-1}$ . Nitrogen adsorption-desorption isotherms were recorded on a volumetric adsorption apparatus (Micromeritics Tristar 3000) at  $-196^\circ\text{C}$ . Samples were outgassed in vacuum at  $150^\circ\text{C}$  for 3 h before measurement. Powder X-ray diffraction (XRD) measurements for the samples were carried out using a Rigaku X-ray diffractometer equipped with high-speed array detection system,  $\text{Cu K}\alpha$  radiation (35 kV and 20 mA) as the X-ray source. XPS analysis was conducted on the PHI Quantum 2000 Scanning ESCA Microprobe using  $\text{Al K}\alpha$  radiation (1846.6 eV) as the X-ray source. Transmission electron microscope (TEM) and high-

resolution TEM (HRTEM) measurements of the catalysts were carried out using a Tecnai F30 electron microscope with a field emission source, operated at an accelerating voltage of 300 kV. HAADF-STEM imaging and EDS elemental analysis were carried out on a Tecnai G2 F30 electron microscope. The electron beam size used for EDS elemental mapping and line-scan is below 2.0 nm. The acquisition time for EDS spectra for individual particles is usually above 10 s, while that for each step of line-scan and two-dimensional mapping is 1.0 s. The EDS spectra for individual particles are used to measure the chemical composition, while the line-scan profiles and elemental mapping show the variation of Ru or Co. All the EDS analyses are qualitative, rather than quantitative, due to the low EDS counts. HS-LEIS spectra for the samples were obtained on IonTOF Qtac100 low-energy ion scattering analyzer, taken with a  $^{20}\text{Ne}^+$  beam energy of 5 keV, with a sample current of 1.6 nA.

### **(3) Benzene hydrogenation Reaction**

The benzene hydrogenation reaction was performed in a stainless steel high pressure reactor (Parr 4848). The mixture of benzene (10 mL) and catalyst (50 mg) was added into the reactor and then it was quickly installed. The reactor was purged with  $\text{N}_2$  for 1 min and then with  $\text{H}_2$  for 1 min. Hydrogen was introduced into the reactor until the pressure reached 4.8 MPa, with a stirring rate of 500 rpm. Then the reactants were quickly heated to 60 °C, and the pressure increased to 5.3 MPa. After the desired reaction time reaching, the autoclave was quickly cooled down to about 5 °C in an ice-water bath and residual hydrogen was evacuated. The products were analyzed by gas chromatography (GC) on a Shimadzu GC 2010 instrument equipped with a DB-35 60 m $\times$ 0.32 mm capillary column and a flame ionization detector (FID) and gas chromatography~mass spectrometry (GC~MS) on a Shimadzu GC~MS 2010. The TOF (turnover frequency) of the catalyst was calculated on the basis of the mols of total metal. The metal dispersion was not calculated for most of the supported catalysts of the liquid benzene hydrogenation in the reported references (as shown in Table S2). For comparison, the metal dispersion of the catalysts was not calculated in this investigation. In fact, the TOF of the catalyst will increase if metal dispersion was

considered.

## 2. TG analysis for the $\text{Co}(\text{OH})_2$ and $\text{Co}/\text{Co}(\text{OH})_2/\text{C}$ samples

The TG-DTG curves of  $\text{Co}(\text{OH})_2$  and  $\text{Co}/\text{Co}(\text{OH})_2/\text{C}$  samples are displayed in Fig. S1. The weight loss at around 88 °C could be attributed to the removal of physically adsorbed water. Another obvious weight reduction appeared at about 210 °C, due to the decomposition of cobalt hydroxide ( $\text{Co}(\text{OH})_2$ ) to cobaltic oxide ( $\text{Co}_3\text{O}_4$ ) and water. Another weight loss occurring at 471 °C for the  $\text{Co}/\text{Co}(\text{OH})_2/\text{C}$  sample, probably assigning to oxidation cobalt reduced by carbon.

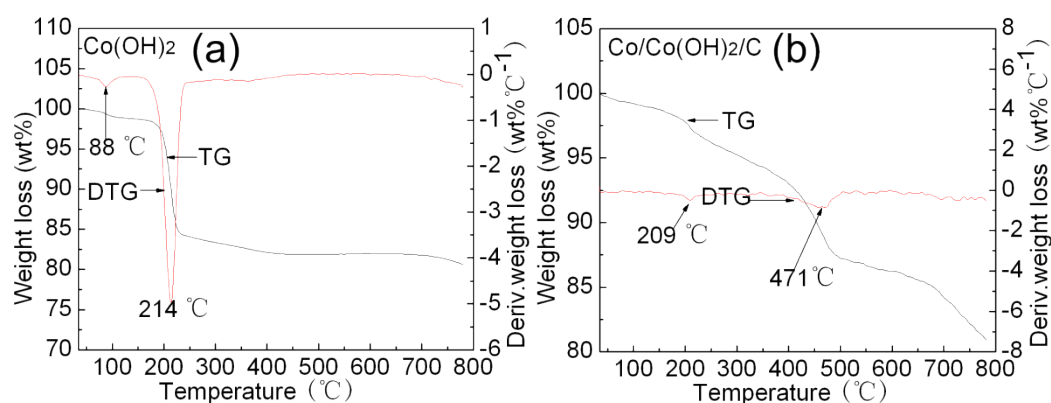


**Fig. S1.** TG-DTG curves of the (a)  $\text{Co}(\text{OH})_2$  and (b)  $\text{Co}/\text{Co}(\text{OH})_2/\text{C}$  samples. The black and red lines represent the thermogravimetry and corresponding differential thermogravimetry curves, respectively.

## 3. BET results of the samples

Table S1 lists the structure parameters (BET surface areas, pore volumes and mean pore diameters) of the samples. The surface area reduced from 1385.3  $\text{m}^2 \text{g}^{-1}$  to 1198.9  $\text{m}^2 \text{g}^{-1}$  after  $\text{Co}/\text{Co}_3\text{O}_4$  loaded on carbon, simultaneously, the mean pore diameter and pore volume decreased because some of pores were occupied by  $\text{Co}/\text{Co}_3\text{O}_4$  NPs. Similarly, the BET surface area, pore volumes and mean pore diameters of Ru-Co bimetallic supported catalysts ( $\text{Ru}/\text{Co}/\text{Co}_3\text{O}_4/\text{C}$  and  $\text{Ru-Co}/\text{C}$ ) were smaller than

carbon. Fig. S2a shows the nitrogen adsorption-desorption isotherm for the Ru/Co/Co<sub>3</sub>O<sub>4</sub>/C catalyst, it is typical for mesoporous materials. The pore size distribution of the Ru/Co/Co<sub>3</sub>O<sub>4</sub>/C catalyst is present in Fig. S2b. The pore size is mainly distributed at 2 nm.

**Table S1:** Structure parameters-BET surface area, pore volume, mean pore radius for different samples.

Sample	$S_{\text{BET}}$ ( $\text{m}^2 \text{g}^{-1}$ ) <sup>[a]</sup>	$V_a$ ( $\text{cm}^3 \text{g}^{-1}$ ) <sup>[b]</sup>	$r_p$ (nm) <sup>[c]</sup>
Carbon	1385.3	1.91	2.75
Co/Co <sub>3</sub> O <sub>4</sub> /C	1198.9	1.49	2.48
Ru-Co/C	1085.2	1.45	2.56
Ru/Co/Co <sub>3</sub> O <sub>4</sub> /C	1126.0	1.39	2.46

[a] BET surface area; [b] Pore volume; [c] Mean pore radius.

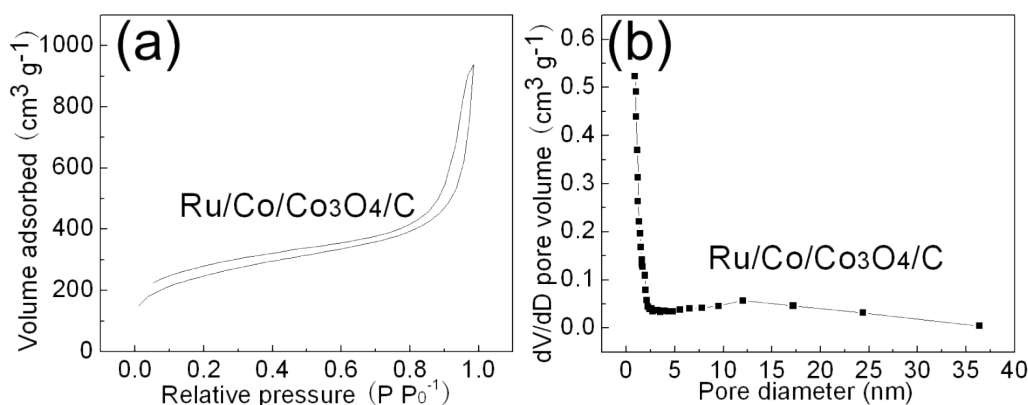


**Fig. S2.** (a) N<sub>2</sub> adsorption-desorption isotherm and (b) pore size distribution for the Ru/Co/Co<sub>3</sub>O<sub>4</sub>/C catalyst.

#### 4. XRD patterns for the samples

Fig. S3 shows the XRD patterns for carbon, Co/Co<sub>3</sub>O<sub>4</sub>/C, Ru-Co/C, Ru/Co/Co<sub>3</sub>O<sub>4</sub>/C and Ru-Co/C~480 samples. The characteristic diffraction peaks of carbon (002) and carbon (100)<sup>1-3</sup> can be clearly observed (Fig. 3A), the other two peaks position at  $2\theta = 36.8^\circ$  and  $2\theta = 44.5^\circ$  could be attributed to (311) and (400)

facets of  $\text{Co}_3\text{O}_4$  in the XRD patterns for the  $\text{Co}/\text{Co}_3\text{O}_4/\text{C}$  and  $\text{Ru}/\text{Co}/\text{Co}_3\text{O}_4/\text{C}$  samples,<sup>4,5</sup> respectively. But no diffraction peak for Ru metal is observed, indicating that Ru NPs are either very small or amorphous in the  $\text{Ru}/\text{Co}/\text{Co}_3\text{O}_4/\text{C}$  catalyst, with a high dispersion. However, there is only one characteristic diffraction peak corresponding to Ru-Co nanoalloy in the XRD patterns for the Ru-Co/C sample. In order to further confirm the formation of Ru-Co nanoalloy in the Ru-Co/C catalyst, the  $\text{Ru}/\text{Co}/\text{Co}(\text{OH})_2/\text{C}$  was reduced in flowing  $\text{N}_2+10\%\text{H}_2$  of  $80 \text{ mL min}^{-1}$  at  $480 \text{ }^\circ\text{C}$  for 3 h, denoted as Ru-Co/C~480. And the XRD patterns for the Ru-Co/C~480 sample is shown in Fig. 3B, exhibiting the typical diffraction peaks of face-center cubic crystals Co (Co(111)) (JCPDS card No. 15-0806) and hexagonal close-packed crystals Ru (Ru(100) and Ru(002)) (JCPDS card No. 06-0663), suggesting the presence of Ru-Co phase segregation. The diffraction peak position at around  $44^\circ$  in the XRD patterns for the Ru-Co/C catalyst located between that of the Ru(002) and Co(111) planes, further demonstrating that the formation of Ru-Co nanoalloy.

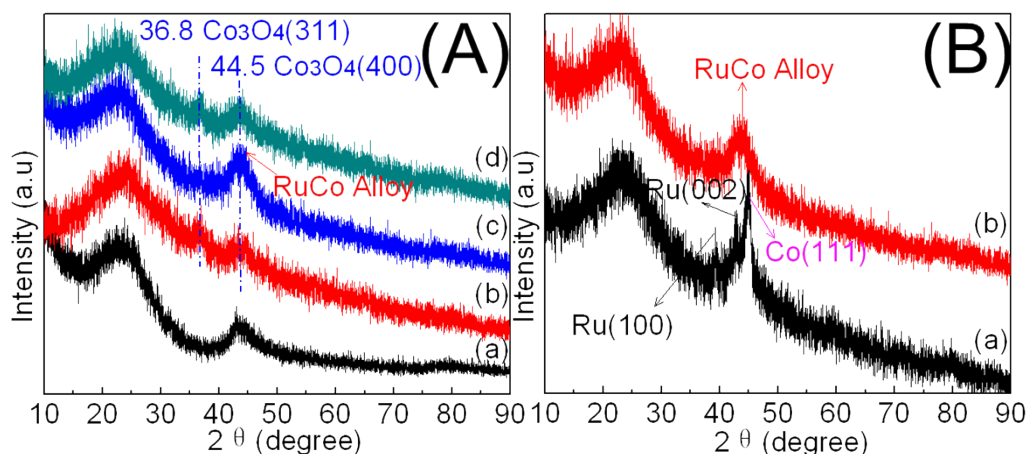


**Fig. S3.** X-ray diffraction (XRD) patterns for the samples. (A) (a) carbon, (b) Co/Co<sub>3</sub>O<sub>4</sub>/C, (c) Ru-Co/C and (d) Ru/Co/Co<sub>3</sub>O<sub>4</sub>/C. (B) (a) Ru-Co/C~480 and (b) Ru-Co/C. The blue dash-dot lines represent the diffraction peaks positions of Co<sub>3</sub>O<sub>4</sub> species. And the magenta, red and black arrows respectively represent the characteristic diffraction peaks of Co, Ru-Co nanoalloy and Ru. These patterns are the raw data recorded on the Rigaku Ultima IV X-ray diffractometer, without any other treatment (such as background subtraction and smoothing). Because Ru or Co content in the as-prepared catalysts is relatively low, NPs are so small or amorphous and well dispersed on carbon, the XRD signals is weak.

## 5. TEM images and NPs size distribution for Co/Co<sub>3</sub>O<sub>4</sub>/C, Ru/C and Ru/Co/Co<sub>3</sub>O<sub>4</sub>/C samples

Fig. S4 shows the typical transmission electron microscopy (TEM) images and the corresponding NPs size distributions for the Co/Co<sub>3</sub>O<sub>4</sub>/C, Ru/C and Ru/Co/Co<sub>3</sub>O<sub>4</sub>/C samples. The mean size of Co/Co<sub>3</sub>O<sub>4</sub>, Ru and Ru/Co/Co<sub>3</sub>O<sub>4</sub> NPs in the Co/Co<sub>3</sub>O<sub>4</sub>/C, Ru/C and Ru/Co/Co<sub>3</sub>O<sub>4</sub>/C samples is about 2.46 nm, 2.43 nm and 2.77 nm, respectively. The NPs in these samples are with narrow size distributions.

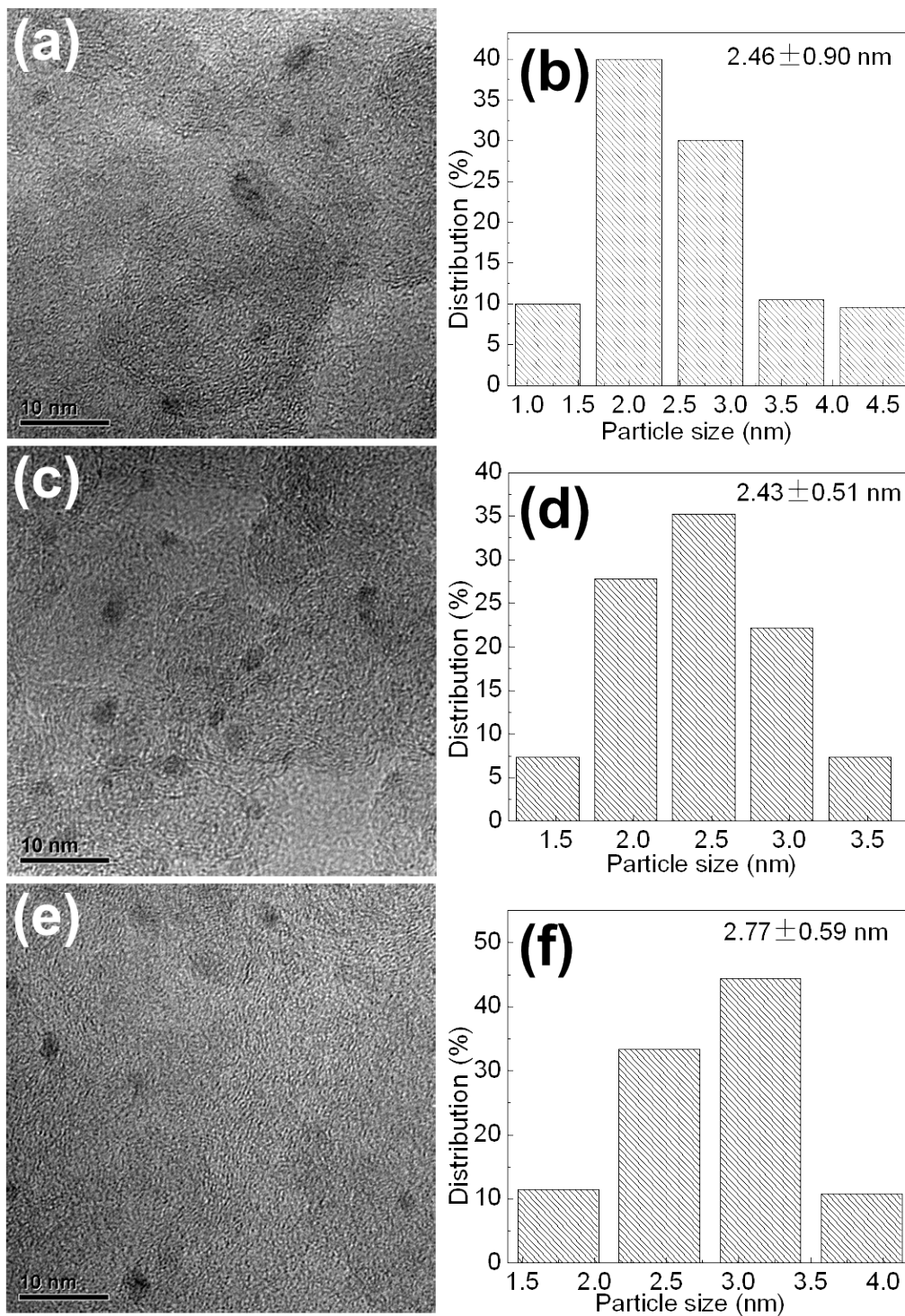


**Fig. S4.** TEM image and Co/Co<sub>3</sub>O<sub>4</sub> NPs size distribution for the (a, b) Co/Co<sub>3</sub>O<sub>4</sub>/C, (c, d) Ru/C and (e, f) Ru/Co/Co<sub>3</sub>O<sub>4</sub>/C samples.

## 6. HAADF-STEM image and elemental analysis for the Ru/Co/Co<sub>3</sub>O<sub>4</sub>/C catalyst

Fig. S5 shows a HAADF-STEM image for the Ru/Co/Co<sub>3</sub>O<sub>4</sub>/C sample and corresponding EDS line-scan results for Ru, Co, O and C. It is clear that all the three nanoparticles have higher Ru concentration, as indicated by the corresponding peaks in the profile of EDS counts for Ru in Fig. S5b. But, it is strange to see that no obvious variation of EDS counts for Co is detected by line-scan, since there is an obvious Co K-peak on the EDS spectrum shown in Fig. 2b in the manuscript when the electron beam is focused on individual nanoparticles. This is attributed to the short acquisition time of ~1.0 s for each step during the EDS line-scan, in order to minimize the effect of specimen drift on the one-to-one correlation between the measured composition and the selected nanoparticles. The results of line-scan indicate that the concentration of Ru is higher than that of Co in the three particles. The variation of EDS counts of carbon is a result of changes in local thickness of the carbon matrix.

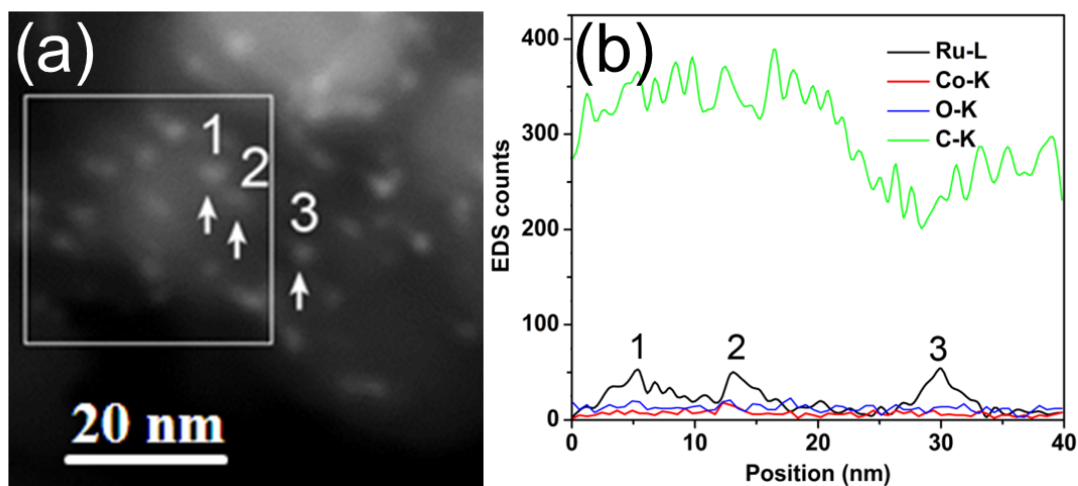


**Fig. S5.** (a) HAADF-STEM image for the Ru/Co/Co<sub>3</sub>O<sub>4</sub>/C sample. (b) composition line profiles obtained by energy-dispersive X-ray spectroscopy (EDS) with an electron beam scanning across the three Ru/Co/Co<sub>3</sub>O<sub>4</sub> NPs “1”-“3” indicated by arrows, green (C), black (Ru), red (Co) and blue (O).

## 7. XPS spectra for the samples

Fig. S6A displays the Co 2p XPS spectrum for the Co/Co<sub>3</sub>O<sub>4</sub>/C, Ru/Co/Co<sub>3</sub>O<sub>4</sub>/C and Ru-Co/C samples. It can be found that the main cobalt species on the surface of the samples are oxidation state Co (Co<sub>3</sub>O<sub>4</sub> and CoOOH).<sup>6-9</sup> However, for the Ru-Co/C catalyst, the content of Co(0) is obviously much higher than the other two samples due to being reduced in N<sub>2</sub>+10%H<sub>2</sub>.

Fig. S6B shows the Ru 3p XPS spectra for the Ru/C, Ru/Co/Co<sub>3</sub>O<sub>4</sub>/C, and Ru-Co/C samples. For the Ru/C and Ru/Co/Co<sub>3</sub>O<sub>4</sub>/C samples (Fig. S6Ba,b), the Ru 3p peak located at 463.2 eV is corresponding to the co-existence of Ru(0) and RuO<sub>2</sub>.<sup>10-12</sup> The presence of RuO<sub>2</sub> was maybe due to the surface oxidation of Ru(0) NPs after being exposed to air prior to measurement.<sup>13</sup> And Ru(0) content on the surface of the Ru-Co/C sample is much larger than that in the Ru/Co/Co<sub>3</sub>O<sub>4</sub>/C or Ru/C sample. The shift towards higher binding energy (Ru(0)-462.2 eV) can be observed for the Ru-Co/C sample (Fig. S6Bc) relative to the monometallic Ru-based catalyst (462 eV), indicating the formation of Ru-Co alloy in the Ru-Co/C sample. Although XPS signal for the samples is weak, due to the low loading of metal and small NPs with good dispersion, the above conclusions has been further identified by HRTEM, HAADF-STEM, EDS-elemental mapping and line-scan, and HS-LEIS results for these samples.

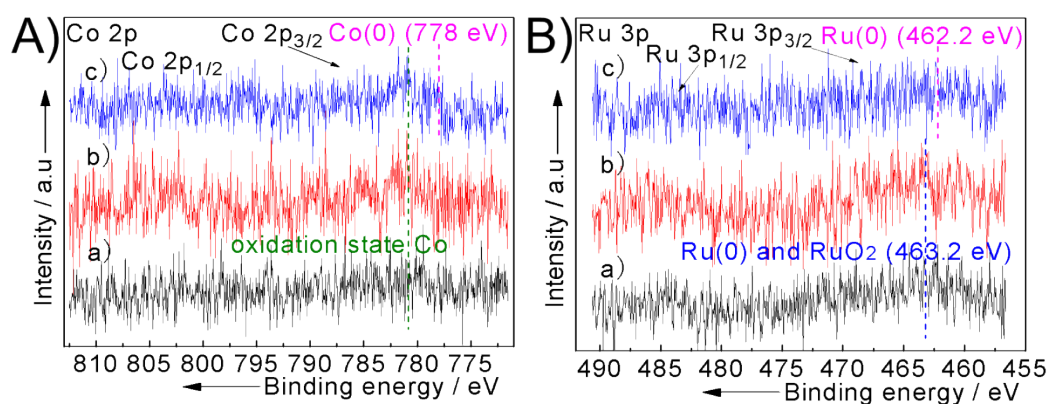
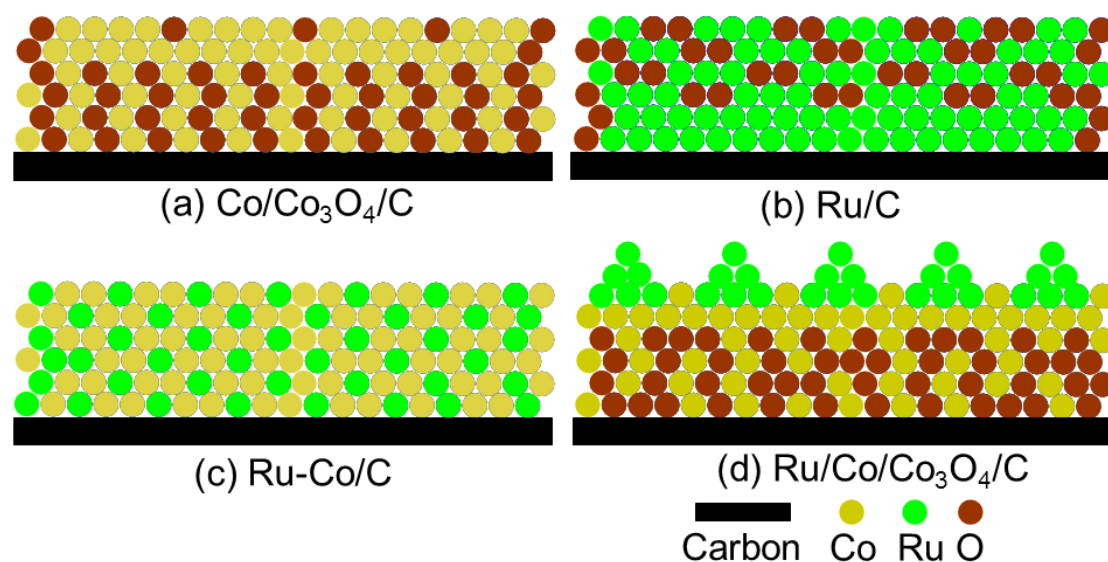


**Fig. S6.** XPS spectrum for the samples. A) Co 2p edge in the a) Co/Co<sub>3</sub>O<sub>4</sub>/C, b) Ru/Co/Co<sub>3</sub>O<sub>4</sub>/C and c) Ru-Co/C sample. B) Ru 3p edge in the a) Ru/C sample, b)

Ru/Co/Co<sub>3</sub>O<sub>4</sub>/C and c) Ru-Co/C sample.

## 8. The schematic models for different samples

The schematic models for different samples are shown in Scheme S2. Scheme S2a demonstrates that the Co is mainly with the form of the oxidation state and Co(0) is loaded on the Co<sub>3</sub>O<sub>4</sub> NPs. A large quantity of RuO<sub>2</sub> is present in Ru/C (Scheme S2b). Ru-Co nanoalloy NPs exist in the Ru-Co/C sample (Scheme S2c). The Ru isolated nanocluster are supported on the Co/Co<sub>3</sub>O<sub>4</sub> surface for the Ru/Co/Co<sub>3</sub>O<sub>4</sub>/C sample (Scheme S2d).



**Scheme S2.** Schematic models for (a) Co/Co<sub>3</sub>O<sub>4</sub>/C, (b) Ru/C, (c) Ru-Co/C and (d) Ru/Co/Co<sub>3</sub>O<sub>4</sub>/C samples, side view.

## 9. Catalytic performance of other unsupported and supported metallic catalysts for benzene hydrogenation to cyclohexane reported in literatures

As listed in Table S2, our Ru/Co/Co<sub>3</sub>O<sub>4</sub>/C catalyst shows quite high catalytic activity for benzene hydrogenation to cyclohexane among a number of supported or

unsupported Ru-based, Rh-based, Pd-based, Ir-based and bimetallic catalysts under similar reaction conditions. The high catalytic activity of this catalyst is mainly contributed to the synergetic effect of multiple catalytic sites (Ru, Co and Co<sub>3</sub>O<sub>4</sub>).

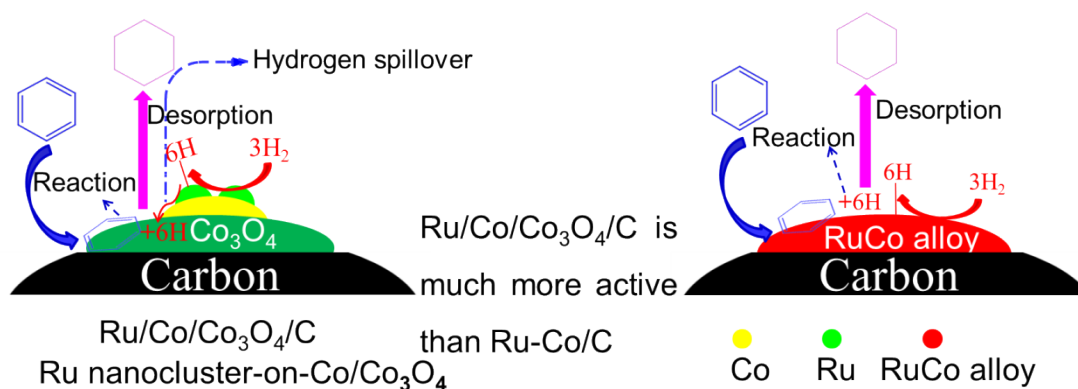
**Table S2:** Catalytic performance of other unsupported and supported metal catalysts for benzene hydrogenation to cyclohexane in the reported literatures.

Ref	Catalyst	t (h)	P (H <sub>2</sub> ) (MPa)	T (°C)	TOF (h <sup>-1</sup> )	Yield <sup>a</sup>
14	[H <sub>4</sub> Ru <sub>4</sub> (η <sup>6</sup> -C <sub>6</sub> H <sub>6</sub> ) <sub>4</sub> ][BF <sub>4</sub> ] <sub>2</sub> <sup>14</sup>	2.5	6.0	90	364	100%
15	2mol%Perfluoro-tagged Ru <sup>15</sup>	0.5	0.1	60	29	34%
16	Ru NPs@SBA-15 <sup>16</sup>	2.5	6.0	110	4000	100%
17	1.4%Ru(0)-Zeolite-Y <sup>17</sup>	1	0.28	22	1040	100%
18	4.2wt%Ru/C-silica <sup>18</sup>	0.53	8.0	110	37700	99.8%
19	4.6wt%Ru/MCF-C <sup>19</sup>	1	4.0	130	17000	19.8%
19	4.6%Ru/rGO <sup>19</sup>	1	4.0	130	38000	61.3%
13	3.3wt%Ru/MMT <sup>13</sup>	2.5	8	110	4000	100%
20	Ru/CNTs <sup>20</sup>	0.5	4.0	80	6983	99.97%
21	0.27%Ru/NFS <sup>21</sup>	2.25	0.29	25	5430	100%
22	0.1wt%Pd/SiO <sub>2</sub> <sup>22</sup>	2	0.83	140	10000	14%
23	Rh/HEA-C16 <sup>23</sup>	5	0.1	20	60	100%
24	11.2wt%Rh/MWNTs <sup>24</sup>	3	1	20	1038	80%
25	Ir NPs <sup>25</sup>	14	0.1	25	91	100%
26	Ir NPs@zeolite <sup>26</sup>	8	0.3	25	3190	100%
27	0.7wt%Rh(cod)-9.86wt%Pd/SiO <sub>2</sub> <sup>27</sup>	2	3	40	1241	52%
28	6.3wt%Pd-6.9wt%Rh/CNT <sup>28</sup>	24	1	20	592.6	100%
29	Rh <sub>0.5</sub> Ni <sub>0.5</sub> <sup>29</sup>	7	4.0	25	290	50.8%
30	Pt-Rh/MWNTs <sup>30</sup>	3	1	20	1953	100%
This work	Ru/Co/Co <sub>3</sub> O <sub>4</sub> /C	0.2	5.3	60	91051.5	100%

<sup>a</sup>Yield to cyclohexane.

## 10. Proposed mechanisms for benzene hydrogenation to cyclohexane

The proposed mechanisms for benzene hydrogenation to cyclohexane over the Ru/Co/Co<sub>3</sub>O<sub>4</sub>/C and Ru-Co/C catalysts are shown in Scheme S3.



**Scheme S3.** Proposed mechanisms for benzene hydrogenation to cyclohexane over the Ru/Co/Co<sub>3</sub>O<sub>4</sub>/C and Ru-Co/C catalysts.

## References

- 1 M. Endo, Y. A. Kim, T. Takeda, S. H. Hong, T. Matusita, T. Hayashi and M. S. Dresselhaus, *Carbon*, 2001, **39**, 2003–2010.
- 2 H.-B. Zhang, G.-D. Lin, Z.-H. Zhou, X. Dong and T. Chen, *Carbon*, 2002, **40**, 2429–2436.
- 3 U. G. Hong, J. K. Kim, J. Lee, J. K. Lee, J. H. Song, J. Yi and I. K. Song, *Appl. Catal. A*, 2014, **469**, 466–471.
- 4 F. Jiao and H. Frei, *Angew. Chem. Int. Ed.*, 2009, **48**, 1841–1844.
- 5 G. P. Gardner, Y. B. Go, D. M. Robinson, P. F. Smith, J. Hadermann, A. Abakumov, M. Greenblatt and G. C. Dismukes, *Angew. Chem. Int. Ed.*, 2012, **51**, 1616–1619.
- 6 W. S. Epling, G. B. Hoflund, J. F. Weaver, S. Tsubota and M. Haruta, *J. Phys. Chem.*, 1996, **100**, 9929–9934.
- 7 A. n. Martínez, C. López, F. Márquez and I. Díaz, *J. Catal.*, 2003, **220**, 486–499.
- 8 Y. Liang, Y. Li, H. Wang, J. Zhou, J. Wang, T. Regier and H. Dai, *Nat. Mater.*, 2011, **10**, 780–786.
- 9 S. Tominaka, T. Momma and T. Osaka, *Electrochim. Acta*, 2008, **53**, 4679–4686.
- 10 N. Chakroune, G. Viau, S. Ammar, L. Poul, D. Veautier, M. M. Chehimi, C. Mangeney, F. Villain and F. Fiévet, *Langmuir*, 2005, **21**, 6788–6796.
- 11 Y. Yamauchi, T. Ohsuna and K. Kuroda, *Chem. Mater.*, 2007, **19**, 1335–1342.
- 12 K. Lasch, L. Jörissen and J. Garche, *J. Power Sources*, 1999, **84**, 225–230.
- 13 S. Miao, Z. Liu, B. Han, J. Huang, Z. Sun, J. Zhang and T. Jiang, *Angew. Chem. Int. Ed.*, 2006, **45**, 266–269.

- 14 P. J. Dyson, D. J. Ellis, T. Welton and D. G. Parker, *Chem. Commun.*, 1999, 25–26.
- 15 S. Niembro, S. Donnici, A. Shafir, A. Vallribera, M. L. Buil, M. A. Esteruelas and C. Larramona, *New J. Chem.*, 2013, **37**, 278–282.
- 16 J. Huang, T. Jiang, B. Han, W. Wu, Z. Liu, Z. Xie and J. Zhang, *Catal. Lett.*, 2005, **103**, 59–62.
- 17 M. Zahmakiran and S. Özkar, *Langmuir*, 2008, **24**, 7065–7067.
- 18 F. Su, L. Lv, F. Y. Lee, T. Liu, A. I. Cooper and X. S. Zhao, *J. Am. Chem. Soc.*, 2007, **129**, 14213–14223.
- 19 K. X. Yao, X. Liu, Z. Li, C. C. Li, H. C. Zeng and Y. Han, *ChemCatChem*, 2012, **4**, 1938–1942.
- 20 Y. Ma, Y. Huang, Y. Cheng, L. Wang and X. Li, *Appl. Catal. A*, 2014, **484**, 154–160.
- 21 M. Zahmakiran, Y. Tonbul and S. Özkar, *J. Am. Chem. Soc.*, 2010, **132**, 6541–6549.
- 22 O Domínguez-Quintero, S Martínez, Y. Henríquez, L. D’Ornelas, H. Krentzien and J. Osuna, *J. Mol. Catal. A*, 2003, **197**, 185–191.
- 23 J. Schulz, A. Roucoux and H. Patin, *Chem. Eur. J.*, 2000, **6**, 618–624.
- 24 H.-B. Pan and C. M. Wai, *J. Phys. Chem. C*, 2009, **113**, 19782–19788.
- 25 V. Mévellec, A. Roucoux, E. Ramirez, K. Philippot and B. Chaudret, *Adv. Synth. Catal.*, 2004, **346**, 72–76.
- 26 Y. Tonbul, M. Zahmakiran and S. Özkar, *Appl. Catal. B*, 2014, **148–149**, 466–472.
- 27 P. Barbaro, C. Bianchini, V. Dal Santo, A. Meli, S. Moneti, C. Pirovano, R. Psaro, L. Sordelli and F. Vizza, *Organometallics*, 2008, **27**, 2809–2824.
- 28 B. Yoon, H.-B. Pan and C. M. Wai, *J. Phys. Chem. C*, 2009, **113**, 1520–1525.
- 29 H. Duan, D. Wang, Y. Kou and Y. Li, *Chem. Commun.*, 2013, **49**, 303–305.
- 30 H.-B. Pan and C. M. Wai, *New J. Chem.*, 2011, **35**, 1649–1660.